Z. Phys. C - Particles and Fields 16, 13-25 (1982)

Zeitschrift für Physik C Particles and Fields

Angular Correlations in $\gamma\gamma \to \rho^0\rho^0$ Near Threshold

TASSO Collaboration

M. Althoff, W. Braunschweig, K. Gather, F.J. Kirschfink, K. Lübelsmeyer, H.-U. Martyn, G. Peise, J. Rimkus, H.G. Sander, D. Schmitz, H. Siebke, D. Trines, W. Wallraff

I. Physikalisches Institut der RWTH Aachen, D-5100 Aachen, Federal Republic of Germany[7]

H. Boerner[4], H.M. Fischer, H. Hartmann, E. Hilger, W. Hillen, G. Knop, L. Köpke, H. Kolanoski, R. Wedemeyer, N. Wermes, M. Wollstadt

Physikalisches Institut der Universität Bonn, D-5300 Bonn, Federal Republic of Germany[7]

H. Burkhardt, S. Cooper, J. Franzke, H. Hultschig, P. Joos, W. Koch, U. Kötz, H. Kowalski[1], A. Ladage, B. Löhr, D. Lüke, P. Mättig, K.H. Mess, D. Notz, J. Pyrlik, D.R. Quarrie[3], R. Riethmüller, W. Schütte, P. Söding, G.Wolf, G. Yekutieli[2]

Deutsches Elektronen-Synchrotron, DESY, D-2000 Hamburg, Federal Republic of Germany

M. Dittmar, R. Fohrmann, H.L. Krasemann, P. Leu, E. Lohrmann, D. Pandoulas, G. Poelz, O. Römer[5], P. Schmüser, B.H. Wiik

II. Institut für Experimentalphysik der Universität Hamburg, D-2000 Hamburg, Federal Republic of Germany[7]

I. Al-Agil, R. Beuselinck, D.M. Binnie, A.J. Campbell, P.J. Dornan, D.A. Garbutt, T.D. Jones, W.G. Jones, S.L. Lloyd, J. McCardle, J.K. Sedgebeer

Department of Physics, Imperial College, London, SW7 2BZ, England[8]

K.W. Bell[3], M.G. Bowler, I.C. Brock, R.J. Cashmore, R. Carnegie, P.E.L. Clarke, R. Devenish, P. Grossmann, J. Illingworth, G.L. Salmon, J. Thomas, T.R. Wyatt, C. Youngman

Department of Nuclear Physics, Oxford University, Oxford, England[8]

B. Foster, J.C. Hart, J. Harvey, J. Proudfoot, D.H. Saxon, P.L. Woodworth

Rutherford Appleton Laboratory, Chilton, Didcot, Oxon OX11 0QX, England[8]

D. Heyland, M. Holder

Gesamthochschule Siegen, D-5900 Siegen, Federal Republic of Germany

E. Duchovni, Y. Eisenberg, U. Karshon, G. Mikenberg, D. Revel, E. Ronat, A. Shapira

Weizmann Institute, Rehovot, Israel[9]

T. Barklow, T. Meyer[6], G. Rudolph, H. Venkataramania, E. Wicklund, Sau Lan Wu, G. Zobernig

Department of Physics, University of Wisconsin, Madison, WI 53706, USA[10]

Received 22 September 1982

1 On leave at CERN, Geneva, Switzerland
2 Minerva Fellow, on leave from Weizmann Institute, Rehovot, Israel
3 On leave from Rutherford Appleton Laboratory, Chilton, England
4 Now at KEK, Oho-Machi, Japan
5 Now at SCS, Hamburg, Germany
6 Now at Texas A+M University, Texas, USA
7 Supported by the Deutsches Bundesministerium für Forschung und Technologie
8 Supported by the UK Science and Engineering Research Council
9 Supported by the Minerva Gesellschaft für Forschung mbH
10 Supported by the US Department of Energy contract WY-76-C-02-0881

0170-9739/82/0016/0013/$02.60

Abstract. We present an analysis of $\rho^0\rho^0$ production by two photons in the $\rho^0\rho^0$ invariant mass range from 1.2 to 2.0 GeV. From a study of the angular correlations in the process $\gamma\gamma \to \rho^0\rho^0 \to \pi^+\pi^-\pi^+\pi^-$ we exclude a dominant contribution from $J^P = 0^-$ or 2^- states. The data indicate sizeable contributions from $J^P = 0^+$ for four pion masses $M_{4\pi} < 1.7$ GeV and from $J^P = 2^+$ for $M_{4\pi} > 1.7$ GeV. The data are also well described by a model with isotropic production and uncorrelated isotropic decay of the ρ^0's. The cross section stays high below the nominal $\rho^0\rho^0$ threshold, i.e. $M_{4\pi} < 1.5$ GeV. The matrix element for $\rho^0\rho^0$ production is found to decrease steeply with increasing $M_{4\pi}$. Upper limits for the couplings of the $\iota(1440)$ and $\Theta(1640)$ to $\gamma\gamma$ and $\rho^0\rho^0$ are given: $\Gamma(\iota \to \gamma\gamma) \cdot B(\iota \to \rho^0\rho^0) < 1.0$ keV and $\Gamma(\Theta \to \gamma\gamma) \cdot B(\Theta \to \rho^0\rho^0) < 1.2$ keV (95% c.l.).

1. Introduction

Two photon collisions observed at e^+e^- storage rings provide excellent means for a detailed exploration of hadronic systems with total angular momentum $J \neq 1$, and even charge conjugation. This includes the study of resonances as well as non-resonant exclusive channels [1–4].

In a previous paper [3] we reported on the first observation of the reaction

$$\gamma\gamma \to \rho^0\rho^0 \to \pi^+\pi^-\pi^+\pi^-. \quad (1)$$

The cross section showed a large enhancement near threshold. This observation has been confirmed [4].

The behaviour of the cross section near threshold has led to various theoretical speculations [5, 6], which in most cases explain the enhancement by the formation of a resonance decaying into $\rho^0\rho^0$. Some authors suggested that a new exotic state has been found which does not fit into the usual quark model scheme, such as a glueball or a four-quark state. One can test for resonance formation by analyzing the angular correlations in the $\pi^+\pi^-\pi^+\pi^-$ final state. In this paper we present a detailed partial wave analysis of reaction (1).

The data were taken with the TASSO detector at the e^+e^- storage ring PETRA at beam energies of 7 GeV, 11 GeV, and between 15 and 18.3 GeV for a total integrated luminosity of 40,900 nb^{-1}. We investigated the four pion mass region $1.2 < M_{4\pi} < 2.0$ GeV extending the measured range of $M_{4\pi}$ below the nominal $\rho^0\rho^0$ threshold.

In Sect. 2 we describe the detector and the data selection. In Sect. 3 we present the Monte Carlo description of the processes leading to a four pion final state. Section 4 explains the fit procedure. In Sect. 5 the results of the spin-parity analysis are presented and discussed. Finally, in Sect. 6 we discuss the cross sections.

2. Detector and Data Selection

At e^+e^- storage rings reaction (1) is observed as a subprocess of

$$e^+e^- \to e^+e^-\pi^+\pi^-\pi^+\pi^-. \quad (2)$$

Detection of the scattered e^+ or e^- was not required in this analysis. The pions were observed in the central detector which is described elsewhere [7].

2.1. Triggers

The data used in this analysis were taken with three different triggers, all based on the central proportional and drift chamber processors which find charged tracks with polar angles ϑ (with respect to the beam direction) satisfying $|\cos\vartheta| < 0.82$ and with momenta, p_t, perpendicular to the beam axis exceeding a selectable minimum. This minimum was set to nominal values p_t^{NOM} of 320 or 220 MeV/c for different running periods. In the vicinity of p_t^{NOM} the efficiency of the processor to find a track is strongly dependent on p_t. For p_t^{NOM} of 220 MeV/c, e.g. this efficiency is 50% at 170 MeV/c, 90% at the nominal value of 220 MeV/c and reaches a constant value of about 95% at 290 MeV/c.

The three triggers were:

(1) the "majority" trigger requiring 4 tracks found by the processor,

(2) the "coplanarity" trigger requiring 2 processor tracks with associated signals in inner time-of-flight counters separated by more than 154°,

(3) the "cathode" trigger requiring two processor tracks and an event vertex within approximately 15 cm of the interaction point along the direction of the beams. The event vertex was found using the cathode information of the central proportional chamber with a measured efficiency of (96.5 ± 0.5)%.

The first half of the data (16,500 nb^{-1}) was taken with triggers 1 and 2 and a setting of the processor mostly to 320 MeV/c. For the second half (24,400 nb^{-1}) trigger 3 was added and the processor was set to 220 MeV/c. This resulted in an increase of the acceptance for 4 prong events by almost a factor of 3 (to about 6% for isotropic $\rho^0\rho^0$ production at $M_{4\pi} = 1.6$ GeV) and made the analysis, especially of the angular distributions, much less sensitive to trigger biases.

2.2. Data Selection

After track reconstruction charged tracks were accepted if they satisfied the following requirements:

1. The track is reconstructed in three dimensions,
2. $d_0 < 5$ cm, where d_0 is the distance of closest approach to the origin in the plane perpendicular to the beam axis,
3. $p_t > 0.100$ GeV/c, where p_t is the momentum transverse to the beam axis,
4. $|\cos\vartheta| < 0.87$.

Candidate events for reaction (1) were selected according to the following criteria:

1. They had to have exactly 2 positive and 2 negative tracks.
2. The z coordinate of the event vertex had to be $|z_v| < 5$ cm (z = axis along the beam).
3. In order to stay within the range of well measured efficiencies we required for the run period with the additional trigger 3 at least 2 out of the 4 tracks to have $p_t > 0.200$ GeV/c and $|\cos\vartheta| < 0.80$. For the run period with triggers 1 and 2 only, all 4 tracks had to fulfill this requirement.

The exclusive $\pi^+\pi^-\pi^+\pi^-$ channel was separated from events with additional undetected particles using the fact that in $e^+e^- \to e^+e^-\gamma\gamma \to e^+e^-X$ the photons are emitted predominantly along the beam direction, giving the system X a low net momentum transverse to the beam axis. For events with four charged tracks Fig. 1a shows the distribution of $|\sum \mathbf{p}_t|^2$, the square of the net transverse momentum. The distribution peaks sharply at zero, indicating the presence of exclusive events, and is flat at higher $|\sum \mathbf{p}_t|^2$. We selected exclusive events by requiring $|\sum \mathbf{p}_t| < 150$ MeV/c. A background from events with missing particles is expected to be flat near $|\sum \mathbf{p}_t|^2 = 0$, as confirmed by the $|\sum \mathbf{p}_t|^2$ distribution for events with five charged particles detected (Fig. 1b). An inspection of the event vertex distribution and the identification of protons showed that beam-gas scattering does not contaminate our data sample. From time-of-flight measurements we know that the number of remaining charged kaons or protons in our sample is negligible.

Assigning pion masses to all particles we obtain the $\pi^+\pi^-\pi^+\pi^-$ mass distribution shown in Fig. 2. The momentum resolution of the tracks was $\sigma_p/p = 0.017\sqrt{1+p^2}$ (p in GeV/c) giving a $M_{4\pi}$ mass resolution of approximately 25 MeV (r.m.s.) in the mass range of interest. The region $1.2 < M_{4\pi} < 2.0$ GeV contains 1,722 events. The background from events with missing particles is estimated by extrapolating the high-

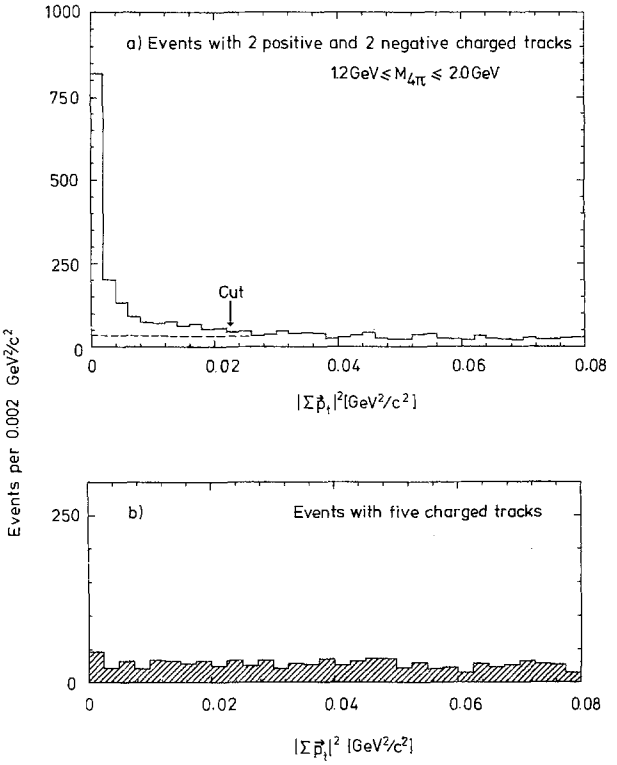

Fig. 1. a $|\sum \mathbf{p}_t|^2$, the square of the transverse momentum of the detected four particle system; **b** $|\sum \mathbf{p}_t|^2$ for events with five particles detected

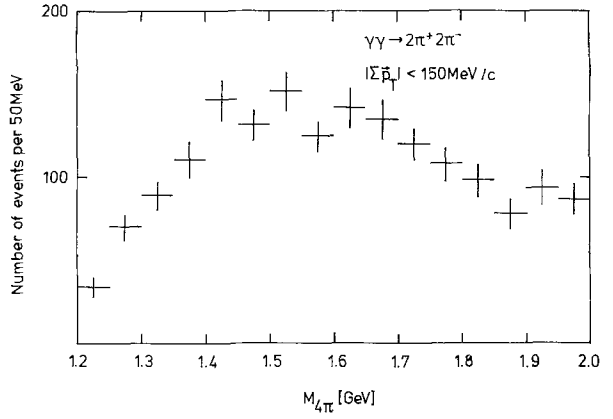

Fig. 2. Invariant mass of the four pion events with $|\sum \mathbf{p}_t| < 150$ MeV

$|\sum \mathbf{p}_t|^2$-tail in Fig. 1a under the peak to be approximately 290 events ($17\% \pm 4\%$). The contribution of one-photon events to this background was found by Monte Carlo simulation to be negligible.

2.3. Evidence for $\rho^0\rho^0$

Figure 3 contains scatter plots of one $\pi^+\pi^-$ mass vs. the other (two entries per event) for different $M_{4\pi}$

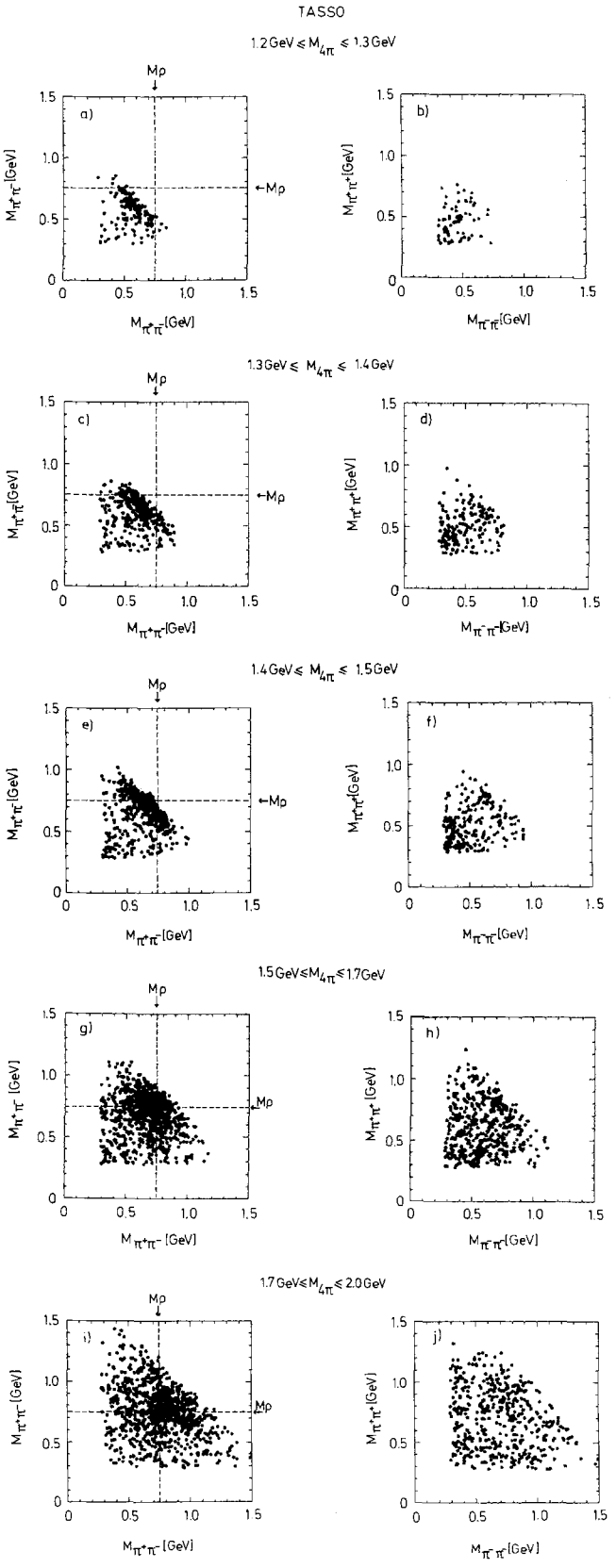

Fig. 3a–j. I) $\pi^+\pi^-$ mass vs. $\pi^+\pi^-$ mass for five different $M_{4\pi}$ intervals (**a, c, e, g, i**). II) The same as I) for $\pi^+\pi^+$ mass vs. $\pi^-\pi^-$ mass (**b, d, f, h, j**)

intervals. For $M_{4\pi}$ larger than the $\rho^0\rho^0$ threshold (Fig. 3g, i) one observes a strong enhancement in the $\rho^0\rho^0$ mass region. This is not seen in the corresponding scatter plots of the like sign mass combinations (one entry per event) shown in Fig. 3h, j. Below the $\rho^0\rho^0$ threshold the enhancement in the unlike sign mass combinations (Fig. 3a, c, e) is shifted towards smaller masses because of the phase space limitations.

3. Parametrization of the Differential Cross Section for $\gamma\gamma \to \pi^+\pi^-\pi^+\pi^-$

To determine the $\rho^0\rho^0$ fraction in our $\pi^+\pi^-\pi^+\pi^-$ sample we fitted a sum of non-interfering contributions from $\rho^0\rho^0$, $\rho^0\pi^+\pi^-$, and four pion phase space to the data using a maximum likelihood method. The probabilities used to define the likelihood function are proportional to the differential cross sections for the various contributions to the $\pi^+\pi^-\pi^+\pi^-$ final state. The parametrization of the differential cross sections is described in the following.

The spin-parity of the $\rho^0\rho^0$ contribution was investigated using a formula for the differential cross section which includes the angular dependence of the production and decay of the ρ^0's as expected from the spin-parity states $J^P = 0^+$, 0^-, 2^+, and 2^-. For comparison we also considered a model in which production and decay of the ρ^0's were isotropic and uncorrelated.

The cross section $\sigma_{\gamma\gamma\to 4\pi}$ in reaction (1) is related to the observed number of events N as a function of the energy $W_{\gamma\gamma}$ of the $\gamma\gamma$-system by

$$\frac{dN}{dW_{\gamma\gamma}} = \int d\omega\, d\xi\, \Phi(W_{\gamma\gamma}, \omega) \frac{d\sigma_{\gamma\gamma\to 4\pi}(W_{\gamma\gamma}, \xi)}{d\xi} A(W_{\gamma\gamma}, \omega, \xi) \quad (3)$$

where the symbol ω represents the variables of the $\gamma\gamma$-system other than $W_{\gamma\gamma}$, and ξ represents the variables describing the $\pi^+\pi^-\pi^+\pi^-$ system. Φ is the differential two-photon flux factor and A is the detection efficiency. The flux was calculated as in [8] and also contains ρ^0 pole form factors to account for the virtuality of the two photons.

At fixed $W_{\gamma\gamma}$, $d\sigma_{\gamma\gamma\to 4\pi}/d\xi$ depends on a set of seven variables which we write symbolically as ξ:

$$\xi = (m_{12}^2, m_{34}^2, \vartheta_\rho^{12}, \vartheta_\pi^{12}, \varphi_\pi^{12}, \vartheta_\pi^{34}, \varphi_\pi^{34}).$$

The four pions are numbered $\pi_1^+, \pi_2^-, \pi_3^+$, and π_4^-. Then m_{ij} denotes the invariant mass of the two pions i and j, ϑ_ρ^{ij} is the angle of the ij system with respect to the $\gamma\gamma$ axis in the $\gamma\gamma$ CM-system (for the event reconstruction a good approximation of the unknown $\gamma\gamma$ axis is the direction of the incoming

electrons), ϑ_π^{ij} and φ_π^{ij} are the polar and azimuthual angles of the pion i in the CM of system ij. Since the scattered electrons were not detected the overall azimuthal dependence of $\rho^0\rho^0$ production (φ_ρ^{12}) has been integrated out.

The seven-fold differential cross section can be written as

$$\frac{d\sigma}{d\xi} = \frac{1}{16\pi^2 W_{\gamma\gamma}^2} W_4(\xi) |(g(\xi) g'(W_{\gamma\gamma})|^2 \tag{4}$$

where $W_4(\xi)$ is the four-pion phase space density and $g(\xi)\cdot g'(W_{\gamma\gamma})$ is the matrix element for a particular production mechanism; $g(\xi)$ describes resonance production in the $\pi^+\pi^-$ channel and angular correlations and $g'(W_{\gamma\gamma})$ contains the $W_{\gamma\gamma}$ dependence of the matrix element. In the Monte Carlo simulation the four pions were generated according to phase space and weighted with the desired $|g(\xi)|^2$. In the likelihood fits, $|g(\xi)|^2$ multiplied by the appropriate normalization factor is the probability for an event with the variables ξ to be produced via the given mechanism. The problem is thus reduced to a determination of the functions $g(\xi)$ for the different contributions we wish to consider.

3.1. *Isotropic Production of $\rho^0\rho^0$, $\rho^0\pi^+\pi^-$ and $\pi^+\pi^-\pi^+\pi^-$*

In the case of isotropic $\rho^0\rho^0$ production and uncorrelated isotropic decay of the ρ^0's, $g(\xi)$ contains only the appropriate ρ^0 Breit-Wigner functions. Because the pions with the same charge are identical bosons the function must be symmetric in the two $\rho^0\rho^0$ combinations that can be formed from $\pi^+\pi^-\pi^+\pi^-$. Thus, for isotropic $\rho^0\rho^0$ production (i.e. isotropic production and isotropic and uncorrelated ρ^0 decays) $g(\xi)$ is

$$g_{\rho\rho}^{\text{iso}}(\xi) = 1/\sqrt{2}(\text{BW}(m_{12})\,\text{BW}(m_{34}) + \text{BW}(m_{14})\,\text{BW}(m_{32}))$$

where the ρ^0 Breit-Wigner amplitude BW and the width Γ_ρ are given by [9]

$$\text{BW}(m) = \frac{\sqrt{m_\rho \Gamma_\rho m/p^*}}{\pi(m_\rho^2 - m^2 - i m_\rho \Gamma_\rho)}$$

and

$$\Gamma_\rho = \Gamma_0 \left(\frac{p^*}{p_0^*}\right)^3 \frac{2p_0^{*2}}{p_0^{*2} + p^{*2}},$$

with

$$p^* = \tfrac{1}{2}\sqrt{m^2 - 4m_\pi^2}, \quad p_0^* = \tfrac{1}{2}\sqrt{m_\rho^2 - 4m_\pi^2}$$

and

$$m_\rho = 776 \text{ MeV}, \quad \Gamma_\rho = 155 \text{ MeV [10]}.$$

Possible non-$\rho^0\rho^0$ contributions were described by $\pi^+\pi^-\pi^+\pi^-$ phase space and $\rho^0\pi^+\pi^-$ production for which the g's are:

$$g_{4\pi}(\xi) = 1$$

and

$$g_{\rho\pi\pi}(\xi) = 1/2(\text{BW}(m_{12}) + \text{BW}(m_{34}) + \text{BW}(m_{14}) + \text{BW}(m_{32})).$$

3.2. *States with Specific Spin and Parity*

The matrix elements for $\rho^0\rho^0$ production with definite spin-parity contain angular correlations between the pions. In the following we define the appropriate function $g(\xi)$ for the $\rho^0\rho^0$ spin-parity states $J^P = 0^+, 0^-, 2^+, 2^-$.

The rotational properties of the amplitude ψ of the $\rho^0\rho^0$ final state can be described by a sum of products of three spherical harmonics:

$$\psi^{JP,Jz}(\xi) \propto \sum a_{L,Lz,S12,S34}^{JP,Jz} Y_L^{Lz}(\vartheta_\rho^{12}, \varphi_\rho^{12}) \cdot Y_1^{S12}(\vartheta_\pi^{12}, \varphi_\pi^{12})\, Y_1^{S34}(\vartheta_\pi^{34}, \varphi_\pi^{34}) \tag{5}$$

where the sum is over L and L_z, the total orbital angular momentum of the $\rho^0\rho^0$ system and its projection on the z-axis, and $S12$ and $S34$, the z-projections of the ρ^0 spins; $S12$ ($S34$) refer to the ρ^0 that decays into pions 1 and 2 (3 and 4). The overall dependence on φ_ρ^{12} can be integrated out. Y_L^{Lz} describes the $\rho^0\rho^0$ production angular distribution. Y_1^{S12} and Y_1^{S34} describe the decay distributions of the two ρ^0's. The ρ^0 production angles and orbital angular momentum are defined in the $\gamma\gamma$ CM-system, with the z-axis along the $\gamma\gamma$ direction. The ρ^0 spin and decay angles are defined in the CM-system of each ρ^0 with the z-axis parallel to the z-axis of the $\gamma\gamma$ CM-system.

The coefficients $a_{L,Lz,S12,S34}^{JP,Jz}$ of (5) were derived by examining the possible quantum numbers of the initial and final states, as follows. Both in the $\gamma\gamma$ and the $\rho^0\rho^0$ system, the possible values of the orbital angular momentum, L, are even for even parity and odd for odd parity states. Since, within our restricted energy range, higher angular momenta are not expected to contribute, we used only $L=0$ and 1 for the $\rho^0\rho^0$ system. In the $\gamma\gamma$ system the restriction to almost real photons, which cannot have helicity 0, requires a combination of L values. We used the two lowest allowed values in each case (either 0 and 2 or 1 and 3), and obtained restrictions on the projections J_z of the total angular momentum vector on

Table 1. The coefficients $a^{JP,Jz}_{L,Lz,S12,S34}$ of (5) (not normalized)

L	Lz	$S12$	$S34$	0^+	0^-	2^+ $Jz=0$	2^+ $Jz=2$	2^- $Jz=0$
0	0	1	−1	1		1		
0	0	0	0	−1		2		
0	0	−1	1	1		1		
0	0	1	1				1	
1	1	0	−1		1			1
1	1	−1	0		−1			−1
1	0	1	−1		−1			2
1	0	−1	1		1			−2
1	−1	0	1		1			1
1	−1	1	0		−1			−1

the $\gamma\gamma$-axis. Only $J_z=0$ is possible for $J=0$ and $J^P=2^-$. For $J^P=2^+$ the intensity of the $J_z=2$ component is six times larger than the $J_z=0$ component. The resulting coefficients $a^{JP,Jz}_{L,Lz,S12,S34}$ are given in Table 1. They are evaluated in the photon helicity system, i.e. the $\gamma\gamma$ CM-system with the z-axis along the γ direction.

For the states of definite spin-parity the $g(\xi)$ are then

$$g^{JP,Jz}_{\rho\rho}(\xi) = 1/\sqrt{2}\,[\mathrm{BW}(m_{12})\,\mathrm{BW}(m_{34}) \cdot \psi^{JP,Jz}(\vartheta^{12}_\rho, \vartheta^{12}_\pi, \varphi^{12}_\pi, \vartheta^{34}_\pi, \varphi^{34}_\pi) + \mathrm{BW}(m_{14})\,\mathrm{BW}(m_{32}) \cdot \psi^{JP,Jz}(\vartheta^{14}_\rho, \vartheta^{14}_\pi, \varphi^{14}_\pi, \vartheta^{32}_\pi, \varphi^{32}_\pi)].$$

4. The Likelihood Function

A maximum likelihood fit was performed to determine the contributions of the various production mechanisms to the observed $\pi^+\pi^-\pi^+\pi^-$ signal. The likelihood function is defined by

$$\Lambda = \prod_{i=1}^{N} \sum_{j=1}^{n} \lambda_j P_j(\xi_i)$$

with the constraint $\sum_{j=1}^{n} \lambda_j = 1$

where λ_j is the fractional contribution of the process j to the $\pi^+\pi^-\pi^+\pi^-$ rate in a given $M_{4\pi}$ bin (typically 100 MeV wide). The λ_j are the free parameters which are varied in the fit to maximize Λ. The product runs over the N events in the $M_{4\pi}$ bin. The sum is over the n contributions considered in a given fit (up to 6). $P_j(\xi_i)$ is the probability for the detected event i with measured variables ξ_i to be produced via the mechanism j. The probability function for each contribution is normalized so that the integral over the acceptance is 1.

$$P_j(\xi_i) = \frac{A(\xi_i)\, d\sigma_j(\xi_i)/d\xi}{\int A(\xi)\, d\sigma_j(\xi)} = \frac{A(\xi_i)\, W_4(\xi_i)\, |g_j(\xi_i)|^2}{\int A(\xi)\, d\sigma_j(\xi)}$$

where $A(\xi)$ is the acceptance for an event with variables ξ. The integrals over the acceptance were calculated by a Monte Carlo program, which included all detector effects such as the trigger and reconstruction efficiencies, chamber resolutions, energy loss, multiple Coulomb scattering, nuclear interaction, etc. In combining different processes we neglected any interference. Note that only states with the same $\gamma\gamma$ helicity (J_z) and the same parity can interfere. The phase space density W_4 is the same for all processes and can be factorized out of the sum in the definition of the likelihood function. In the absence of smearing effects due to the finite resolution of ξ, $A(\xi)$ is independent of the process considered and was also factorized out. The maximization was performed on the logarithm of the likelihood function with the constant terms dropped, and with a term $-\sum \lambda_j$ which imposes the constraint $\sum \lambda_j = 1$. The resulting function is

$$\log \Lambda' = \sum_{i=1}^{N} \log\left[\sum_{j=1}^{n} \lambda_j |g_j(\xi_i)|^2 / \int d\sigma_j(\xi)\, A(\xi)\right] - \sum_{j=1}^{n} \lambda_j.$$

The fitting procedure was tested extensively. Event samples with mixtures of the various processes were generated with the Monte Carlo program and fitted in the same manner as the data. Without any exception we found that the fit reproduced the input mixture within the errors. This implies that the dependence of smearing effects on the particular production mechanism, as well as the approximation of the actual direction of the γ's by the beam direction, play a minor rôle in this procedure.

5. Results of the Spin-Parity Analysis

The maximum likelihood fits were performed in the range $1.2 < M_{4\pi} < 2.0$ GeV. At higher masses the restriction to the lowest partial waves is probably no longer justified.

The discussion of the fit results is organized as follows. To give a first impression of the spin-parity content of the data, we expand the angular correlations into orthogonal functions and compare the coefficients of this expansion obtained from the data with those obtained from the Monte Carlo simulations of different spin-parity states. Then we present the results of fits with a model where the production of $\rho^0\rho^0$, $\rho^0\pi^+\pi^-$ and $\pi^+\pi^-\pi^+\pi^-$ is described by phase space. These results are compared to a 6-parameter fit where the lowest $\rho^0\rho^0 J^P$ states replace the isotropic $\rho^0\rho^0$ production. We then proceed to discuss the significance of the fits and derive conclusions from the fits to the J^P states.

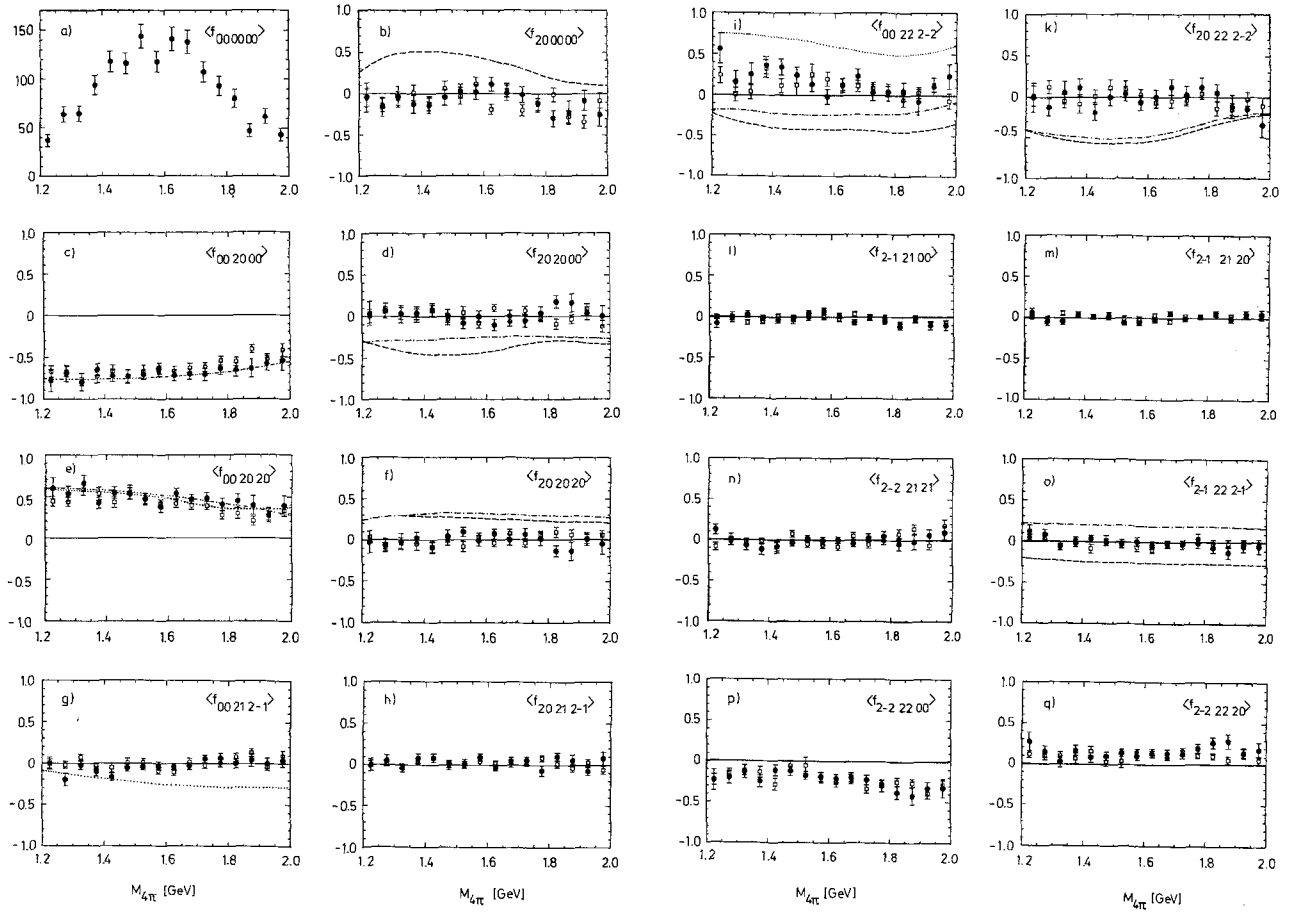

Fig. 4a–q. Moments of the orthogonal functions defined in (6) of the text. No acceptance corrections have been applied to the data (closed circles). Monte Carlo predictions are shown for isotropic $\rho^0\rho^0$ production (open squares) and $\rho^0\rho^0$ production with $J^P=0^+$ (dotted), $J^P=0^-$ (dash-dotted line), $J^P=2^+$ (three-dots-dashed line) and $J^P=2^-$ (dashed line). The curves for the different J^P states are only shown if they are significantly different from the isotropic case

5.1. Expansion of the Angular Correlations Into Orthogonal Functions

In a first approach to investigate the spin-parity contributions we expanded the angular correlations derived from equation (5) into orthogonal functions and compared the coefficients (moments) of the expansion obtained for the data with those of the Monte Carlo simulation. This expansion has the advantage of including correlations which cannot be seen in one-dimensional distributions. Note, however, that the expansion does not include correlations between $\pi\pi$ masses and angles. The orthogonal functions have the form

$$f_{\lambda,\mu,\lambda a,\mu a,\lambda b,\mu b}(\xi)=\tfrac{1}{2}(\sqrt{4\pi})^3\,\mathrm{Re}\{Y^{\mu}_{\lambda}(\vartheta_{\rho a},\varphi_{\rho a}) \times [Y^{\mu a}_{\lambda a}(\vartheta_{\pi a},\varphi_{\pi a})\,Y^{\mu b}_{\lambda b}(\vartheta_{\pi b},\varphi_{\pi b}) + Y^{\mu a}_{\lambda a}(\vartheta_{\pi b},\varphi_{\pi b})\,Y^{\mu b}_{\lambda b}(\vartheta_{\pi a},\varphi_{\pi a})]\} \quad (6)$$

where

$\lambda=0,2,\ldots,\quad \lambda a$ and $\lambda b=0,2$

$|\mu a|\leqq\lambda a$ and $|\mu b|\leqq\lambda b$

$\mu+\mu a+\mu b=0$ and $\mu a\geqq\mu b$.

We used the 16 functions with $\lambda\leqq 2$, corresponding to our restriction to the orbital angular momenta $L=0$ and 1. The comparison was made using events which have at least one of the two possible $\pi^+\pi^- - \pi^+\pi^-$ combinations with both $\pi^+\pi^-$ masses within 150 MeV of the ρ^0 mass; for $1.5<M_{4\pi}<2.0$ GeV 'ρ^0 mass' means the nominal mass; below 1.5 GeV this value is shifted linearly by 50 MeV for every 100 MeV in $M_{4\pi}$. (Throughout this paper we refer to this definition as the ρ band). If an event has two $\rho^0\rho^0$ combinations both enter into the determination of the moments.

In Fig. 4 the moments are plotted as a function of $M_{4\pi}$. No acceptance corrections have been ap-

plied to the data. The moment with all indices zero (Fig. 4a) is unnormalized and gives the number of entries per bin (up to two entries per event). All other moments are normalized to this moment. The data are compared with the Monte Carlo calculation for isotropic $\rho^0\rho^0$ (open squares). The moments for particular spin-parity states are only shown if the Monte Carlo simulation exhibits a significant difference from the isotropic case. Due to the limited angular acceptance the predictions for $J^P = 0^+$, 2^+ generally differ only little from the isotropic case. Exceptions are for $J^P = 0^+$ the moments $\langle f_{00212-1}\rangle$, $\langle f_{00222-2}\rangle$, shown in Fig. 4g, i, where the last one shows the clearest difference from the isotropic case. For 2^+ slight deviations from the isotropic case are seen for $M_{4\pi} > 1.7$ GeV in the moments $\langle f_{002000}\rangle$ and $\langle f_{002020}\rangle$ (Fig. 4c, e). The negative parity states $J^P = 0^-$ and 2^- show clear deviations from the isotropic case in several moments.

Table 2a. Results of the 3-parameter fit. Percentage of observed events attributed to each contribution

$W\gamma\gamma$ [GeV]	$\rho^0\rho^0$-iso	$\rho^0\pi^+\pi^-$	$\pi^+\pi^-\pi^+\pi^-$	$\log \Lambda'$
1.2-1.3	110±20	−37±27	27±17	767.2
1.3-1.4	53±12	11±17	36±12	1,437.4
1.4-1.5	86± 8	−23±10	36± 8	1,996.2
1.5-1.6	62± 9	13±11	25± 6	1,839.5
1.6-1.7	65±10	11±12	24± 7	1,725.4
1.7-1.8	49±11	14±13	37± 8	1,247.0
1.8-1.9	30±12	38±14	31± 8	859.1
1.9-2.0	19±10	25±15	56±10	822.9

Table 2b. Results of the 2-parameter fit. Percentage of observed events attributed to each contribution

$W\gamma\gamma$ [GeV]	$\rho^0\rho^0$-iso	$\rho^0\pi^+\pi^-$	$\pi^+\pi^-\pi^+\pi^-$	$\log \Lambda'$
1.2-1.3	89±20	-	11±17	766.3
1.3-1.4	59±12	-	41±12	1,437.2
1.4-1.5	75± 8	-	25± 8	1,993.8
1.5-1.6	70± 9	-	30± 6	1,838.8
1.6-1.7	71±10	-	29± 7	1,725.0

The isotropic model fits the data well except for a slight discrepancy seen in Fig. 4c, e for $M_{4\pi} > 1.7$ GeV. For the moment where the 0^+ and isotropic predictions differ most (Fig. 4i) the data below 1.7 GeV have the tendency to lie between the two. The 2^+ prediction, which as noted before is very similar to that for isotropy, agrees well with the data, even for $M_{4\pi} > 1.7$ GeV, where the isotropic model does not fit as well. The 0^- and 2^- predictions fail to describe the data in all moments where 0^- and 2^- differ from the isotropic case. Thus the $\rho^0\rho^0$ signal is not dominated by 0^- or 2^- states.

5.2. *Likelihood Fit with Isotropic $\rho^0\rho^0$ Production*

In order to exploit the full information on the angular and mass distributions with all correlations we carried out maximum likelihood fits as described in Sect. 4. The results of such fits to contributions from $\rho^0\rho^0$, $\rho^0\pi^+\pi^-$ and $\pi^+\pi^-\pi^+\pi^-$, where pure phase space production is assumed for all three contributions are given in Table 2a. For each $M_{4\pi}$ bin the fractions of events assigned by the fit to each of the processes are listed.

In the five $M_{4\pi}$ bins from 1.2 to 1.7 GeV the fractions assigned to $\rho^0\pi^+\pi^-$ are consistent with being zero. Therefore the fit was repeated in this region with the $\rho^0\pi^+\pi^-$ fraction set to zero. These results are given in Table 2b. Comparing the values obtained for the likelihood function we conclude that a $\rho^0\pi^+\pi^-$ contribution is not required by the data below 1.7 GeV. We will refer to this fit as the '3-parameter fit' although up to $M_{4\pi} = 1.7$ GeV $\rho^0\pi^+\pi^-$ is not included.

The fractions found for 4-pion phase space are about 30%. From an analysis of the $|\sum \mathbf{p}_t|^2$ distribution (Fig. 1) we determined a background from four pion events with missing particles of about 17% in all $M_{4\pi}$ bins except for the lowest one where it goes up to about 25%. By varying the cut in $|\sum \mathbf{p}_t|$ we found that in the fits the background does not contribute to the fitted $\rho^0\rho^0$ fraction, except in the

Table 2c. Results of the 6-parameter fit. Percentage of observed events attributed to each contribution

$W\gamma\gamma$ [GeV]	$\rho^0\rho^0-\hat{0}^+$	$\rho^0\rho^0-0^-$	$\rho^0\rho^0-2^+$	$\rho^0\rho^0-2^-$	$\rho^0\pi^+\pi^-$	$\pi^+\pi^-\pi^+\pi^-$	$\log \Lambda'$
1.2-1.3	31±12	−7±6	22±17	16±11	27±24	11±17	764.1
1.3-1.4	29± 9	7±5	−2±12	0± 6	39±16	28±12	1,438.6
1.4-1.5	47± 7	8±4	6±10	5± 5	11±10	22± 7	2,000.0
1.5-1.6	23± 7	5±4	7±10	5± 5	42±11	18± 6	1,832.2
1.6-1.7	26± 8	−2±4	15±12	14± 5	27±12	20± 6	1,726.1
1.7-1.8	−2± 8	−2+4	52± 9	−1± 6	18±10	36± 6	1,250.5
1.8-1.9	19±11	−5±4	22±14	3± 6	28±17	32± 8	863.7
1.9-2.0	13±11	4±4	24±12	2± 5	− 2±16	59±10	828.8

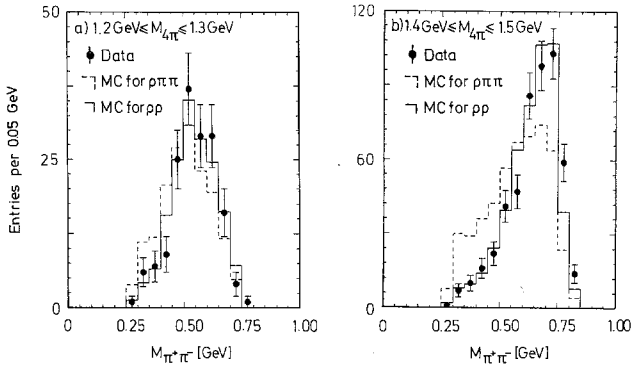

Fig. 5. **a** $\pi^+\pi^-$ mass distribution for $1.2<M_{4\pi}<1.3\,\text{GeV}$. A $\pi^+\pi^-$ combination enters the plot if the other combination is within the ρ-band (see text). Data are compared to a Monte Carlo simulation of $\rho^0\rho^0$ and $\rho^0\pi^+\pi^-$. **b** The same as a) for $1.4<M_{4\pi}<1.5\,\text{GeV}$

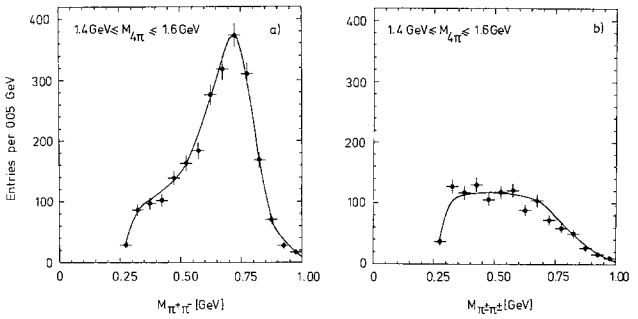

Fig. 6. **a** $\pi^+\pi^-$ mass distribution for $1.4<M_{4\pi}<1.6\,\text{GeV}$ together with the result of the 3-parameter fit (solid curve). **b** The same as a) for $\pi^\pm\pi^\pm$ masses

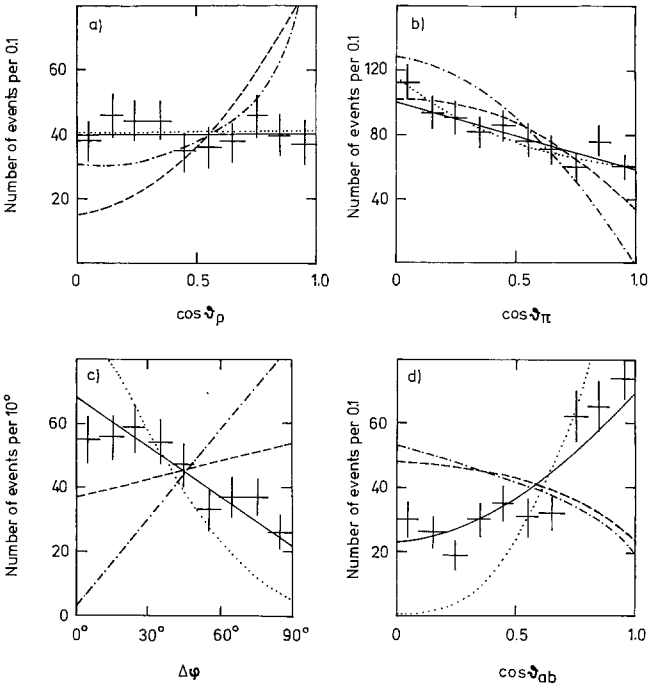

Fig. 7a–d. Angular distributions for $1.4<M_{4\pi}<1.6\,\text{GeV}$. The angles are explained in the text (data = crosses). The solid curve is the result of the 3-parameter fit, the other curves are Monte Carlo predictions for $\rho^0\rho^0$ production with $J^P=2^-$ (dashed line), $J^P=0^-$ (dash-dotted line) or $J^P=0^+$ (dotted). The distribution for $J^P=2^+$ coincides with the curve for the isotropic case (result of the 3-parameter fit)

lowest $M_{4\pi}$ bin where a correction of 13% had to be applied.

As is seen from Tables 2a and b, the $\rho^0\rho^0$ yields are high for $M_{4\pi}$ even below the nominal $\rho^0\rho^0$ threshold. This is in accordance with the distributions in Fig. 3a, c, e showing that the $\rho^0\rho^0$ signal is indeed visible below the nominal $\rho^0\rho^0$ threshold. The behaviour of both the $\pi^+\pi^-$ vs. $\pi^+\pi^-$ and the $\pi^+\pi^+$ vs. $\pi^-\pi^-$ distributions is well reproduced by the Monte Carlo simulation.

We checked that even in the lowest $M_{4\pi}$ bins a distinction between $\rho^0\rho^0$ and $\rho^0\pi^+\pi^-$ production is possible. In Fig. 5a the $\pi^+\pi^-$ masses of events with $1.2<M_{4\pi}<1.3\,\text{GeV}$ are plotted if the other $\pi^+\pi^-$ combination is in the ρ band as defined above. In the same plot the corresponding distribution for $\rho^0\pi^+\pi^-$ and for $\rho^0\rho^0$ as obtained from the Monte Carlo simulation is compared with the data. The peaking of the data towards the ρ^0 mass matches the Monte Carlo distribution for $\rho^0\rho^0$ but not for $\rho^0\pi^+\pi^-$. For larger $M_{4\pi}$ (Fig. 5b) the effect is even more pronounced.

To demonstrate the quality of the fit we compare in Figs. 6 and 7 for the mass range $1.4<M_{4\pi}<1.6\,\text{GeV}$ the mass and angular distributions of our data with those from Monte Carlo simulations. The Monte Carlo distributions include the effect of the acceptance. For the angular distributions those events were considered which had both $\pi^+\pi^-$ masses in the ρ^0 band (as defined above) for at least one $\pi^+\pi^- - \pi^+\pi^-$ combination. If both $\pi^+\pi^- - \pi^+\pi^-$ combinations are within this cut, they both appear in the plots. The polar angle ϑ_ρ of the ρ^0 production axis (Fig. 7a) is defined in the $\gamma\gamma$ CM system with the z-axis along the $\gamma\gamma$-axis. For the Figs. 7b and c, the angles ϑ_π and φ_π describing the ρ^0 decay are taken in the ρ^0 helicity frames, which are the ρ^0 rest systems with the positive z-axis in the direction of flight of one of the ρ^0's. ϑ_π is the polar angle of the π^+ from a ρ^0 (Fig. 7b). $\Delta\varphi=\varphi_{\pi a}-\varphi_{\pi b}$ is the angle between the decay planes of the $2\rho^0$'s (denoted as a and b) (Fig. 7c). ϑ_{ab} is the opening angle between the two π^+ directions, each defined in its respective ρ^0 CM frame (Fig. 7d). The solid curves in Figs. 6 and 7 show the result of the 3-parameter fit, i.e. with isotropic $\rho^0\rho^0$. They describe the data well.

5.3. Fits to Different Spin Parity States

For the analysis of the spin parity content of the $\rho^0\rho^0$ channel a fit was made allowing for 6 contributions: the four $\rho^0\rho^0$ partial waves with $J^P = 0^+$, 0^-, 2^+, and 2^- together with $\rho^0\pi^+\pi^-$ and $\pi^+\pi^-\pi^+\pi^-$. The results of this 6-parameter fit are given in Table 2c.

An important result of the fit is that the contributions of the negative parity states 0^- and 2^- are small (with a possible exception around 1.4 GeV). This is in agreement with the moment analysis discussed above. It also agrees with the angular distributions shown in Fig. 7. In these plots the $J^P = 0^-$ and 2^- states are predicted to show distinct features which are not observed in the data. The most striking discrepancies are found for the correlations $\Delta\varphi$ and $\cos\vartheta_{ab}$. Thus, the dominance of negative parity states suggested by several authors [5] to explain the large $\rho^0\rho^0$ cross section at low $M_{4\pi}$ is excluded.

The results on the positive parity states can be summarized as follows: For low $M_{4\pi}$ masses, $M_{4\pi} < 1.7$ GeV, the fitted $\rho^0\rho^0$ contribution has dominantly $J^P = 0^+$ while the 2^+ fraction is small. At higher masses the 2^+ contribution appears to become dominant. These conclusions are in agreement with the moment analysis which indicates a noticable 0^+ contribution in Fig. 4i and the presence of 2^+ above $M_{4\pi} = 1.7$ GeV in Fig. 4c, e. Remember, however, that in the moments the positive parity contributions are less distinct from the isotropic case than the negative parity states (see above). Of course, the likelihood analysis is superior since it takes into account all correlations between the final state particles, in particular those arising from the symmetrization.

5.4. Comparison of the Fits

The fit with isotropic $\rho^0\rho^0$ production, which has two (three) free parameters for $M_{4\pi} < 1.7$ GeV (> 1.7 GeV), gives as good a description of the data as the fit with different J^P states (6 free parameters). It is conceivable that the choice of partial waves considered in the latter fit is too restrictive and that additional $\rho^0\rho^0$ contributions are included by the fit in the isotropic $\rho^0\rho^0$ contribution*. For low $M_{4\pi}$ masses, $M_{4\pi} < 1.7$ GeV, the total $\rho^0\rho^0$ fraction obtained by the 6-parameter fit is systematically lower than in the isotropic case; the difference is particularly large for $1.3 < M_{4\pi} < 1.4$ GeV and $1.5 < M_{4\pi} < 1.6$ GeV. The size of the difference indicates the uncertainty in extracting the $\rho^0\rho^0$ contribution.

* Under the assumption that the two initial state photons are real the total J_z and therefore the J_z values of the final state ρ^0's are restricted; as a result an isotropic configuration seems to be impossible to construct by summing different states

Table 3. χ^2 per degree of freedom (n_D) for $\pi^+\pi^-$ and $\pi^\pm\pi^\pm$ mass distributions and for the 16 moments. Data are compared to the 3 and 6-parameter fits (n_D is the number of bins minus 1 for the overall normalisation; n_D is the same for the 3 and 6-parameter fits.).

$W_{\gamma\gamma}$ [GeV]	Mass distributions			Moments	
	χ^2/n_D		n_D	χ^2/n_D,	$n_D = 15$
	3 param	6 param		3 param	6 param
1.2–1.3	1.77	2.53	23	0.62	0.77
1.3–1.4	1.74	1.72	27	1.45	1.21
1.4–1.5	1.25	1.25	31	1.07	0.49
1.5–1.6	1.11	1.53	35	1.02	1.15
1.6–1.7	0.71	0.85	40	0.99	0.85
1.7–1.8	1.13	1.20	43	1.33	1.48
1.8–1.9	1.09	1.18	46	4.25	2.49
1.9–2.0	0.83	0.84	51	0.69	0.50

5.5. One-Dimensional Distributions

We proceed to show that both the 3 and the 6-parameter fit give a good description of the data. The value of the likelihood function alone represents no absolute measure of the quality of the fit. Therefore we compare the Monte Carlo simulation of the fit with the data in one-dimensional mass and angular distributions. In Table 3 we list the χ^2 per degree of freedom for the $\pi^+\pi^-$ one-dimensional mass distributions and the 16 moments separately for the 3 and 6-parameter fits. Examples for mass and angular distributions are shown in Figs. 6 and 7. Both, the figures and the χ^2 values indicate good agreement with the data. Exceptions are to some extent the mass distributions in the lowest two bins and especially the moment in the bin from 1.8 to 1.9 GeV, where both the 3 and the 6-parameter fits fail.

6. Determination of Cross Sections

In order to calculate cross sections a Monte Carlo integration of (3) was performed for each of the production mechanisms separately. For a cross section of 1 nb and a two-photon flux corresponding to the measured integrated luminosity, the expected numbers of detected events per $M_{4\pi}$ bin of 25 MeV are shown in Fig. 8. These curves were used to obtain cross sections for $\rho^0\rho^0$ production in the region $1.2 < M_{4\pi} < 2.0$ GeV from the results of the 3-parameter (Table 4a) and 6-parameter fits (Table 4b). The cross sections resulting from the fit to isotropic

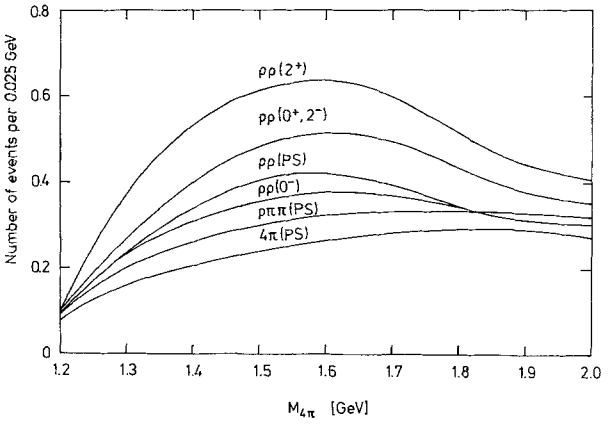

Fig. 8. Number of events per 25 MeV bin in $M_{4\pi}$ expected from Monte Carlo simulations for the different models assuming a $\gamma\gamma$ cross section of 1 nb for 4-pion production and a two-photon flux corresponding to the measured integrated luminosity

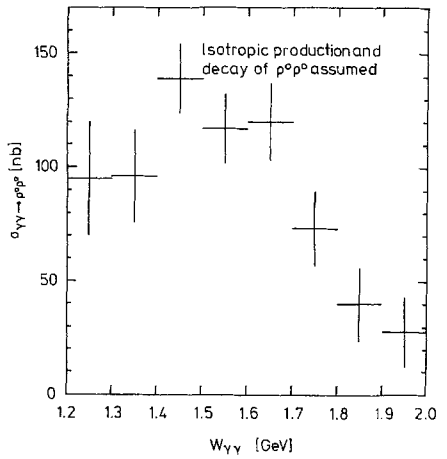

Fig. 9. Cross section for $\gamma\gamma \to \rho^0\rho^0$. The efficiency is calculated assuming isotropic $\rho^0\rho^0$ production (Table 4a). Note that the systematic uncertainty is substantial (see text)

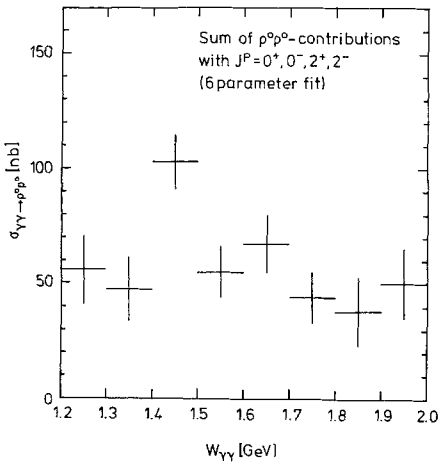

Fig. 10. Cross sections for $\gamma\gamma \to \rho^0\rho^0$ calculated as the sum of the different spin parity contributions from Table 4b

Table 4a. Results of the 3(2)-parameter fit. Cross sections in nanobarn

$W\gamma\gamma$ [GeV]	$\rho^0\rho^0$-iso	$W\gamma\gamma$ [GeV]	$\rho^0\rho^0$-iso
1.2–1.3	95±25	1.6–1.7	120±13
1.3–1.4	96±15	1.7–1.8	73±16
1.4–1.5	139±10	1.8–1.9	40±15
1.5–1.6	117±11	1.9–2.0	28±15

Table 4b. Results of the 6-parameter fit. Cross sections in nanobarn

$W\gamma\gamma$ [GeV]	$\rho^0\rho^0-0^+$	$\rho^0\rho^0-0^-$	$\rho^0\rho^0-2^+$	$\rho^0\rho^0-2^-$
1.2–1.3	31±12	− 8±8	18±14	16±11
1.3–1.4	38±11	12±9	− 2±13	0± 8
1.4–1.5	71±11	17±9	7±12	8± 7
1.5–1.6	32±10	9±7	8±11	7± 7
1.6–1.7	35±11	− 4±7	17±13	19± 7
1.7–1.8	− 3±10	− 3±6	51± 9	− 1± 6
1.8–1.9	21±12	− 6±5	20±13	3± 6
1.9–2.0	16±13	6±7	25±13	3± 6

$\rho^0\rho^0$, $\rho^0\pi^+\pi^-$ and $\pi^+\pi^-\pi^+\pi^-$ are shown in Fig. 9. To obtain the $\rho^0\rho^0$ cross section from the 6-parameter fit the $\rho^0\rho^0$ contributions from the four different J^P states were summed (Fig. 10). The errors given in the figures are those obtained from the fit; no systematic errors are included.

6.1. Systematic Errors

The systematic uncertainty in determining cross sections is substantial, as can be seen from a comparison of the cross section results from the 3 and the 6-parameter fits. The difference in the results has two sources:

- the two fits assign different fractions of events to $\rho^0\rho^0$ production,
- the acceptances for different J^P states and isotropic $\rho^0\rho^0$ are considerably different (see Fig. 8).

The differences in the fit results may be caused by the following reasons:

- the special choice of the ansatz for the differential cross sections,
- the parametrisation of the ρ^0 resonance,
- contributions from higher partial waves not included in the fits,
- contributions from processes not considered in the analysis.

We are not able to resolve these uncertainties within this analysis.

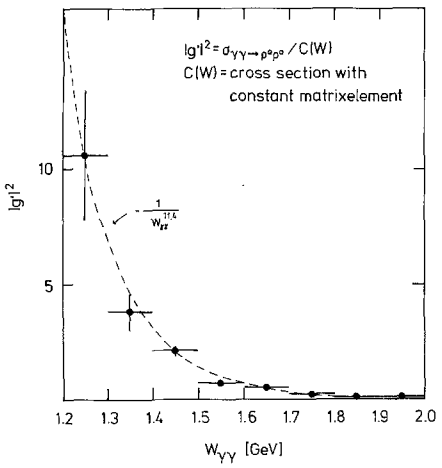

Fig. 11. Square of the matrix element obtained from Fig. 9 as described in the text

Compared to the uncertainties in the fit results the systematic error in the calculation of the detector acceptances for a given four pion production mechanism is small, 12% above $M_{4\pi}=1.5$ GeV rising to about 25% for the lowest mass bin.

6.2. Discussion of the Cross Sections

Within the systematic errors the cross sections presented in Fig. 9, determined for isotropic $\rho^0\rho^0$ production, and in Fig. 10, determined by summing the $\rho^0\rho^0$ contributions from the individual J^P states, are consistent with our published result [3] which was given for $W_{\gamma\gamma}>1.5$ GeV ($W_{\gamma\gamma}=M_{4\pi}$). The cross section is large at the nominal $\rho^0\rho^0$ threshold and even below.

The fact that the cross section is large below the nominal $\rho^0\rho^0$ threshold is surprising because the available phase space decreases drastically. That means that the matrix element responsible for $\rho^0\rho^0$ production has a strong dependence on $W_{\gamma\gamma}$. In Fig. 11 we plot the average $W_{\gamma\gamma}$ dependence of the matrix element squared $|g'(W_{\gamma\gamma})|^2$, which we determined by dividing the measured cross section of Fig. 9 by a cross section obtained by integrating the differential cross section in (4) over the final state variables ξ setting $g'(W_{\gamma\gamma})=1$. The matrix element is found to fall $\sim 1/W_{\gamma\gamma}^n$ with $n=11.4\pm0.6$. Despite the large discrepancies in the cross sections, the matrix element obtained from Fig. 10 has a similar $W_{\gamma\gamma}$ dependence ($n=11.3\pm0.8$).

The behaviour of the matrix element may suggest the presence of the $J^P=2^+$ resonance $f(1\,270)$. Taking the cross section evaluated with the efficiency for $J^P=2^+$ (Table 4b) and the measured $\gamma\gamma$-width of the $f(1\,270)$ [2] a width of $\Gamma(f\to\rho^0\rho^0)>25$ MeV would be required, which is incompatible with the measured value $\Gamma(f\to\pi^+\pi^-\pi^+\pi^-)=(5.0\pm0.8)$ MeV [10]. Contributions from other known resonances have been estimated to be even smaller [5]. For example, we find that the cross section for $\gamma\gamma$ production of the scalar meson $\varepsilon(1\,300)$ and its subsequent decay into $\rho^0\rho^0$ is less than about 5 nb. For this estimate, we used the vector meson dominance model, the upper limit on the coupling of the $\varepsilon(1\,300)$ to $\gamma\gamma$ times the branching ratio into $\pi^+\pi^-$, $\Gamma(\varepsilon\to\gamma\gamma)\cdot B(\varepsilon\to\pi^+\pi^-)<1.5$ keV (for 1,300 MeV $<M_\varepsilon<$ 1,500 MeV) [2] and the assumption that the ε couples dominantly to $\pi\pi$.

It has been pointed out [11] that the glueball candidate state $\iota(1\,440)$ [12], with $M=1{,}440\pm10$ MeV, $\Gamma=55\pm20$ MeV and $J^P=0^-$, could have a relatively large branching ratio to both $\gamma\gamma$ and $\rho^0\rho^0$. In fact, the largest 0^- contribution in Table 4b is in the region of the $\iota(1\,440)$. We determined an upper limit for the product:

$$\Gamma(\iota\to\gamma\gamma)\cdot B(\iota\to\rho^0\rho^0)<1.0\,\text{keV}, \quad (95\%\,\text{c.l.}).$$

Of similar interest is the newly found state $\Theta(1\,640)$ [13] for which we find as an upper limit:

$$\Gamma(\Theta\to\gamma\gamma)\cdot B(\Theta\to\rho^0\rho^0)<1.2\,\text{keV}, \quad (95\%\,\text{c.l.}).$$

7. Summary

From a detailed analysis of the angular correlations in the $\pi^+\pi^-\pi^+\pi^-$ final state at masses $1.2<M_{4\pi}<2.0$ GeV we exclude a dominant contribution from the negative parity states $J^P=0^-$ and 2^- to the reaction $\gamma\gamma\to\rho^0\rho^0$. The data indicate sizeable contributions from $J^P=0^-$ for $M_{4\pi}<1.7$ GeV and from $J^P=2^+$ for $M_{4\pi}>1.7$ GeV. The data are also well described by a model with isotropic production and uncorrelated isotropic decay of the ρ^0's. We have determined cross sections for $\gamma\gamma\to\rho^0\rho^0$ in the range $1.2<M_{4\pi}<2.0$ GeV. We find that the previously observed enhancement around the nominal $\rho^0\rho^0$ threshold extends down to $M_{4\pi}=1.2$ GeV. The corresponding matrix element for $\rho^0\rho^0$ production is steeply decreasing with energy. We determine upper limits for products of radiative width and branching ratio to $\rho^0\rho^0$ for the states $\iota(1\,440)$ and $\Theta(1\,640)$, $\Gamma(\iota\to\gamma\gamma)\cdot B(\iota\to\rho^0\rho^0)<1.0$ keV and $\Gamma(\Theta\to\gamma\gamma)\cdot B(\Theta\to\rho^0\rho^0)<1.2$ keV.

Acknowledgements. We thank the DESY directorate for its continuing support of the experiment. The tremendous efforts of the PETRA machine group are gratefully acknowledged. We thank the DESY Rechenzentrum for providing excellent facilities. Those of us from abroad wish to thank the DESY directorate for the hospitality extended to us while working at DESY.

References

1. G.S. Abrams et al.: Phys. Rev. Lett. **43**, 477 (1979); Ch. Berger et al.: Phys. Lett. **94B**, 254 (1980); A. Roussarie et al.: Phys. Lett. **105B**, 304 (1981); TASSO Collaboration. R. Brandelik et al.: Phys. Lett. **108B**, 67 (1982); C. Edwards et al.: Phys. Lett. **110B**, 82 (1982); CELLO Collaboration. H.J. Behrend et al.: Phys. Lett. **114B**, 378 (1982)
2. TASSO Collaboration. R. Brandelik et al.: Z. Phys. C – Particles and Fields **10**, 117 (1981)
3. TASSO Collaboration. R. Brandelik et al.: Phys. Lett. **97B**, 448 (1980)
4. D.L. Burke et al.: Phys. Lett. **103B**, 153 (1981)
5. H. Goldberg, T. Weiler: Phys. Lett. **102B**, 63 (1981); J. Layssac, F.M. Renard: Montpelier preprint PM/80/11 (1980)
6. R.M. Godbole, K.V.L. Sarma: Phys. Lett. **109B**, 504 (1982); S. Minami: Lett. Nuovo Cimento **34**, 125 (1982); Bing An Li, K.F. Liu: SLAC-PUB-2783 (T/E) (1981); N.N. Achasov, S.A. Devyanin, G.N. Shestakov: Phys. Lett. **108B**, 134 (1982); K. Biswal, S.P. Misra: Bhubaneswar preprints IP/BBSR/80-18 (1980); IP/BBSR/81-13 (1981); IP/BBSR/82-1 (1982)
7. TASSO Collaboration. R. Brandelik et al.: Phys. Lett. **83B**, 261 (1979); Z. Phys. C – Particles and Fields **4**, 87 (1980)
8. J.H. Field: Nucl. Phys. B **168**, 477 (1980) (and Erratum)
9. J.D. Jackson: Nuovo Cimento **34**, 1644 (1964)
10. Particle Data Group, C. Bricman et al.: Phys. Lett. **75B**, (1978)
11. S. Pinsky: Proc. of the XVIIth Rencontre de Moriond, Les Arcs, France, March 20-26 1982
12. C. Edwards et al.: Phys. Rev. Lett. **49**, 259 (1982)
13. C. Edwards et al.: Phys. Rev. Lett. **48**, 458 (1982)